

Nonlinear Driver Parameter Estimation and Driver Steering Behavior Analysis for ADAS Using Field Test Data

Changxi You, Jianbo Lu, and Panagiotis Tsiotras, *Senior Member, IEEE*

Abstract—In the development of advanced driver-assist systems (ADAS) for lane-keeping or cornering, one important design objective is to appropriately share the steering control with the driver. The steering behavior of the driver must therefore be well characterized for the design of a high-performance ADAS controller. This paper adopts the well-known two-point visual driver model to characterize the steering behavior of the driver, and conducts a series of field tests to identify the model parameters and validate this model in real-world scenarios. An extended Kalman filter and an unscented Kalman filter are implemented for estimating the driver parameters using either a joint-state estimation algorithm or a dual estimation algorithm. The estimated parameters for different types of drivers are analyzed and compared. The results show that the two-point visual driver model captures realistic driving behavior with time-varying, but not necessarily constant, parameters. A wavelet analysis of the driver steering command shows that distinct driver classes can be identified by analyzing the smoothness of the driver command using the Lipschitz exponents of the recorded signals.

Index Terms—Extended Kalman filter (EKF), field test, parameter estimation, two-point visual driver model, unscented Kalman filter (UKF), wavelet signal analysis.

I. INTRODUCTION

MORE than six million motor vehicle crashes occurred in the U.S. in 2014 alone, of which 27% resulted in injury or death [1]. From 2014 to 2015, the total number of vehicle crashes increased by 3.8%, and the number of fatal crashes increased by 7% [2]. Another study, sponsored by National Highway Traffic Safety Administration, investigated 723 crashes and showed that driver behavioral error caused or contributed to 99% of these crashes [3]. Given the increased sophistication of

automotive active safety systems, these studies show that driver behavior still remains the most important factor contributing to accidents. It is therefore necessary to understand, characterize and, if possible, predict driver behavior so as to design better, and more proactive (as opposed to merely reactive) advanced driver-assist systems (ADAS). Nevertheless, driver modeling is a difficult task since driver behavior is affected by different individual factors, such as gender, age, experience, and driver's aggression. Such diverse driver behaviors have a significant effect on the performance of ADAS [4], [5]. A controller for vehicle handling stability should take into account the diverse driver skills, habits, and handling behavior of different drivers, and persistently provide good "intuitive" performance. In order to characterize driver behavior, researchers have proposed different driver models based on several methodologies over the past four decades.

Wier and McRuer [6] used transfer functions to describe the result of the driver's actions on the vehicle's position error and yaw angle, and built a quasi-linear model (crossover model) to approximately describe the nonlinear steering behavior of the driver. This model uses feedback control to eliminate the tracking error, but it does not take the driver's preview behavior into consideration. MacAdam [7], [8] assumed that the driver wants to minimize a predefined previewed output error, and modeled the driver's steering strategy as an optimal preview process with a time lag. Hess and Modjtahedzadeh [9], [10] introduced a control-theoretic model for the steering behavior of the driver. This model consisted of a preview component along with low- and high-frequency compensation elements. The above models successfully achieve lane-tracking using only lateral control; braking is not considered in these works. Burgett and Miller [11] designed and optimized a parameterized driver model using a multivariable nonlinear regression approach, based on data collected from test tracks and driving simulations. This model investigated the driver's braking strategy in order to avoid rear-end driving conflicts. Chatzikomis and Spentzas [12] proposed a path-following driver model that regulated both the steering wheel and the throttle/brake by previewing the path ahead of the vehicle. In [13] and [14], model predictive controller (MPC)-based driver steering models have been considered. Keen and Cole [14], in particular, linearized the vehicle model at different working points and used a multimodel structure to characterize the ability of the driver to predict the future vehicle path. By

Manuscript received June 17, 2016; revised February 23, 2017 and April 21, 2017; accepted June 10, 2017. This work was supported by National Science Foundation Awards CMMI-1234286 and CPS-1544814 and the Ford Motor Company. This paper was recommended by Associate Editor Dr. Rafael Toledo. (Corresponding author: Panagiotis Tsiotras)

C. You is with the School of Aerospace Engineering, Georgia Institute of Technology, Atlanta, GA 30332-0150 USA (e-mail: cyou6@gatech.edu).

J. Lu is with the Research and Advanced Engineering, Ford Motor Company, Dearborn, MI 48121 USA (e-mail: jlu10@ford.com).

P. Tsiotras is with the School of Aerospace Engineering and the Institute for Robotics and Intelligent Machines, Georgia Institute of Technology, Atlanta, GA 30332-0150 USA (e-mail: tsiotras@gatech.edu).

Color versions of one or more of the figures in this paper are available online at <http://ieeexplore.ieee.org>.

Digital Object Identifier 10.1109/THMS.2017.2727547

using different combinations of the internal models, this MPC achieves various driver expertise in the path-following task.

The driver's mental work has also been taken into consideration for driver modeling. In [15], Flad *et al.* proposed a steering-primitive optimal selection driver model by defining a set of elementary control primitives to describe the driver's neuromuscular system, limbs, and control actions. This model assumes that the driver has a mental model of the vehicle and the steering task and determines the optimal sequence of control primitives to achieve the target maneuver. Different artificial intelligence approaches have also been introduced to model the driver's mental work and behaviors. In [16], Kageyama and Pacejka evaluated the driver's mental influence from the environment with respect to a "risk level" and proposed a driver model based on fuzzy control theory. Lin *et al.* [17] built a neural network driver model and compared three typical model configurations in great detail. More recently, Hamada *et al.* [18] proposed a beta process autoregressive hidden Markov model (HMM). This model was trained in an unsupervised way using real driving data, and was used to predict the driving behaviors of the drivers.

All previous driver control-theoretic models can be categorized into the following three groups according to the methodology used to develop them.

- 1) Classical control theory such as [6], [9], and [10], where the system is represented using transfer functions and the stability is analyzed using frequency-response methods.
- 2) Modern control theory such as [7], [8], [11], [12], and [14], where the system is represented in state space and the stability is analyzed in the time domain.
- 3) Intelligent control theory such as [16]–[18], where the artificial intelligence approaches including neural network, fuzzy logic, and HMM are used to develop the driver models [19].

These driver models focus on three kinds of driving tasks, including longitudinal control [11], lateral control [6]–[10], [14], [15], [17], and combined longitudinal-lateral control [12], [16], [18].

Recently, nonparameterized models such as neural networks or HMMs have been used to predict driver behavior. They have to be trained offline by using supervised/unsupervised machine learning techniques and they typically need large amounts of data. Furthermore, nonparameterized models are not very transparent to the user and hence are not convenient for designing driver-based ADAS controllers. The parameters of these models are difficult to modify in order to characterize different driving behaviors; instead, the model must be retrained using new data to capture new driver types and driving styles. Parameterized, transfer-function-based driver models, such as the crossover model [6], [20], the control theoretic model [9], and the two-point visual driver model [21]–[23] on the other hand are better for control design tasks, since they are easy to use (they are quasi/linear), and their parameters correspond to measurable physical variables that relate to meaningful performance parameters. Among these driver models, the two-point visual driver model is considered to have both satisfactory model accuracy and good identification feasibility [24].

The two-point visual driver model used in this paper is derived from the concept of the two-level steering mechanism observed in a series of psychological experiments involving human drivers [25]–[27]. In [25], Donges divided the driver's steering task into a guidance level and a stabilization level, and thereby built a two-level steering model. The guidance level interprets the driver's perceptual response with respect to the oncoming road in an anticipatory open-loop control mode. The stabilization level interprets the driver's compensatory behavior with respect to the deviation from the reference path in a closed-loop control mode. This idea has been widely accepted and has been further developed by subsequent researchers [22], [23], [26]–[28]. Among these researchers, Salvucci [23] first introduced the concepts of visual "near point" and "far point" into the model. By taking appropriate choices of the "near point" and "far point," the two-point visual driver model achieves different tasks such as lane tracking [23] and collision avoidance [29].

The contributions of this paper can be summarized as follows: First, the paper adopts the two-point visual driver model from [22], since this model characterizes driver steering behavior more precisely. This driver model combines both a two-level visual strategy and high-frequency kinesthetic feedback. The latter accounts for the interaction between the driver's arms and the steering wheel [9]. Saleh *et al.* in [21], [30], [31] also adopted the two-level visual strategy, but instead of the high-frequency kinesthetic feedback in [9], [22], a well-designed neuromuscular system was used. The identification of the parameters of the model in [30], [31], and [21] was done using simulated data. In this paper, we show the validity of the proposed model by comparing with actual recorded driver data collected during field experiments. Although previous work has validated the two-point visual driver model and identified the driver model parameters using a driving simulator [22], [30], this is the first instance that the model is validated using actual field test data. Second, by applying four different identification methods, namely, the joint extended Kalman filter/unscented Kalman filter (EKF/UKF) and the dual EKF/UKF [32]–[34] it is shown that the model parameters are indeed identifiable using minimal data, but that some of these parameters are not necessarily constant but may vary with time. Our results thus reveal that *parameter-varying* versions of the two-point visual driver model may provide a much better explanation of actual human driver behavior. It is expected that these observations will pave the way for online driver behavior and cognitive driver state identification, which can be used downstream in the ADAS architecture in order to adapt the controller gains to the specific driver/vehicle/traffic configuration. Finally, we show that when comparing different driving types, the smoothness of the driver steering command may be a good discriminating feature for driver classification. Using wavelet signal analysis, it is shown that different driver styles correspond to different signal smoothness (i.e., degree of differentiability), as measured by the rate of decay of the wavelet coefficients. As far as we know, this is the first work that wavelet analysis has been applied to determine driver categories.

The paper is structured as follows. Section II introduces the mathematical modeling of the driver. Section III details the approaches used to identify the driver model parameters, while

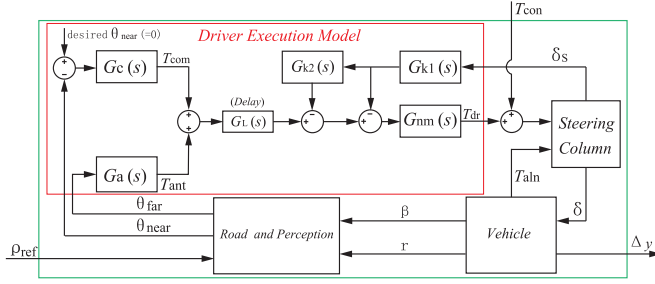


Fig. 1. Human-vehicle-road closed-loop system.

Section IV describes the equipment and the driving scenarios used for the field tests. Section V outlines the data processing task and presents the results. Section VI analyzes and compares different driver styles. Finally, Section VII summarizes the results of this study and provides some directions for future work.

II. SYSTEM MODELING AND PROBLEM FORMULATION

The proposed human-vehicle-road system consists of four subsystems, as shown in Fig. 1.

- 1) The driver model that exerts a steering torque on the steering wheel.

The steering column model that converts steering torque to steering angle;

The vehicle model that provides the necessary position and state information of the vehicle; and

The road and perception model that provides the road geometry and kinematics, and also determines the driver's visual perception angles.

The input to the system is the curvature of the road ρ_{ref} , which can be treated either as an external reference command to be tracked or a disturbance to be rejected, depending on the problem formulation. The primary performance variable is the lateral deviation Δy of the so-called "near point" directly in front of the vehicle to the centerline of the road (see Figs. 1 and 2).

A. Driver Model

We use the driver model proposed in [22], which introduces a kinesthetic force feedback from the steering wheel. The structure of this model is shown in the red rectangular box in Fig. 1. The transfer functions $G_a(s)$ and $G_c(s)$ account for the anticipatory control and the compensatory control actions of the driver, respectively. The system $G_{\text{nm}}(s)$ approximately describes the neuromuscular response of the driver's arms. The "Delay" block indicates the driver's processing delay in the brain, and the transfer functions $G_{k1}(s)$ and $G_{k2}(s)$ account for the driver's kinesthetic perception of the steering system. The variables T_{ant} and T_{com} denote the driver's steering torques corresponding to the anticipatory control and the compensatory control paths, respectively; δ_s denotes the steering wheel angle; and the inputs θ_{near} and θ_{far} denote the near-field and the far-field visual angles, respectively (see Fig. 2). Finally, T_{dr} denotes the driver's total steering torque delivered at the steering wheel. The transfer

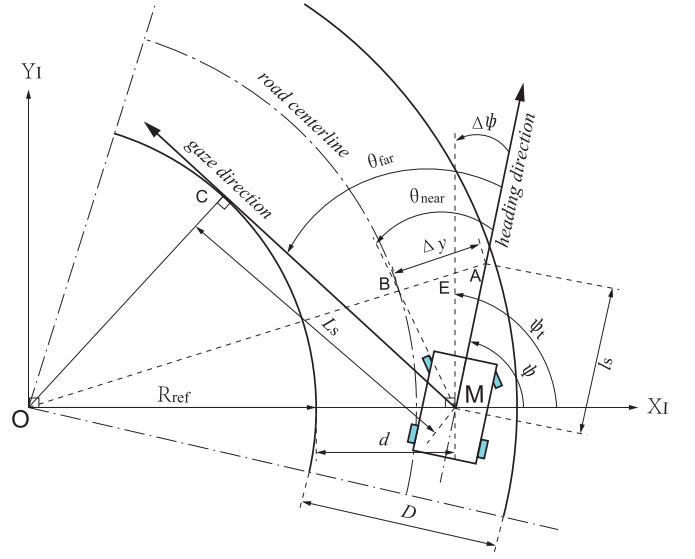


Fig. 2. Road geometries, vehicle states, and driver's visual perception.

functions of the blocks shown in Fig. 1 are given below

$$\begin{aligned} G_a(s) &= K_a, & G_c(s) &= K_c \frac{T_L s + 1}{T_1 s + 1} \\ G_{\text{nm}}(s) &= \frac{1}{T_N s + 1}, & G_{k1}(s) &= K_D \frac{T_{k1} s}{T_{k1} s + 1} \\ G_L(s) &= e^{-t_p s}, & G_{k2}(s) &= K_G \frac{T_{k2} s + 1}{T_{k3} s + 1} \end{aligned} \quad (1)$$

where K_a and K_c are static gains for the anticipatory and compensatory control subsystems, respectively; K_D and K_G are static gains for the kinesthetic perception feedback subsystems, respectively; T_L and T_1 ($T_L > T_1$) are the lead time and lag time constants, respectively; T_{k1} , T_{k2} , and T_{k3} are the three time constants of the driver's kinesthetic perception feedback from the steering wheel, t_p is the delay for the driver to process sensory signals, and T_N is the time constant of the driver's arm neuromuscular system. K_a , K_c , K_D , K_G , T_L , T_1 , T_N , T_{k1} , T_{k2} , T_{k3} , and t_p are the 11 parameters of the driver model.

B. Road and Perception Model

The road and perception model interacts with both the vehicle model and the driver model (refer to Fig. 1) and achieves two functions: 1) It determines the vehicle's position and posture relative to the road geometry; and 2) it determines the location of the driver's near and far visual points on the upcoming road. The near visual point is fixed at a certain distance along the heading direction of the vehicle, while the far visual point is taken as the tangent point on the inner road boundary for driving on a curved road, or the vanishing point of the road for driving along a straight road [23]. Fig. 2 illustrates the relations between the geometry of driver's visual perception, the vehicle and the curved road [35], [36]. In Fig. 2, the frame X_I-O-Y_I is fixed on the road. It is assumed that the vehicle is cornering with a certain lateral deviation from the road centerline. Let ψ denote the vehicle's yaw angle, let ψ_t denote the angle be-

tween the tangent to the road centerline and the X_1 axis, and let M denote the current position of the vehicle's center of mass. Let also A denote the driver's "lookahead" point in front of M at a distance ℓ_s along the vehicle's heading direction, let B denote the intersection of OA with the road centerline, let E denote the intersection of AB with the tangent to the road centerline, and let C denote the point of tangency of the line along the gaze direction on the road's inner boundary. Furthermore, let L_s denote the distance between C and M , let θ_{far} denote the visual angle between the gaze direction of the driver from a far away point and the heading direction of the vehicle, and let θ_{near} denote the near-point visual angle between MB and the heading direction of the vehicle. Finally in Fig. 2, Δy denotes the length of the line segment AB —the predicted deviation from the road centerline at the near lookahead point if the vehicles continues with the current heading, R_{ref} denotes the radius of the road's inner boundary, d denotes the distance from M to the road's inner boundary, and D denotes the width of the road. Henceforth, it will be assumed that d and D are small compared to R_{ref} . From Fig. 2, the near- and far-distance visual perception angles can be approximated as [22], [25], [35]–[38]

$$\theta_{\text{near}} \approx \frac{\Delta y}{\ell_s} \quad (2a)$$

$$\theta_{\text{far}} \approx \frac{L_s}{R_{\text{ref}}} + \Delta\psi \approx L_s \rho_{\text{ref}} + \Delta\psi \quad (2b)$$

where $\rho_{\text{ref}} = 1/R_{\text{ref}}$ is the road curvature, and $\Delta\psi = \psi_t - \psi$ is the angle between the tangent of the road centerline and the vehicle's heading direction.

C. Problem Formulation

We formulate the driver parameter estimation problem based on the driver model, road and perception model, steering column model, and vehicle model summarized in the previous section. For notational simplicity, let $p_1 = K_a$, $p_2 = K_c$, $p_3 = T_L$, $p_4 = T_1$, $p_5 = T_N$, and $p_6 = t_p$. The driver's near-field lookahead distance ℓ_s is also an important feature of the driver steering characteristics. We thus take ℓ_s as an additional parameter, and let $p_7 = \ell_s$. We further let $p_8 = K_D$, $p_9 = K_G$, $p_{10} = T_{k_1}$, $p_{11} = T_{k_2}$, and $p_{12} = T_{k_3}$ for the high-frequency kinesthetic feedback in the driver model. Since the human driver has physical limits, each model

parameter is restricted to lie within some compact interval, $p_i \in [\underline{p}_i, \overline{p}_i]$, $i = 1, 2, \dots, 12$. Let $p = (p_1, p_2, \dots, p_{12})^T \in \mathcal{P} = [\underline{p}_1, \overline{p}_1] \times [\underline{p}_2, \overline{p}_2] \times \dots \times [\underline{p}_{12}, \overline{p}_{12}] \subset \mathbb{R}^{12}$. The upper and lower bounds (\overline{p}_i and \underline{p}_i) that define \mathcal{P} are given in Table III.

The combined system of the driver model and the road and perception model can be written in the form

$$\dot{x}^c = A^c(p)x^c + B^c(p)u^c \quad (3a)$$

$$y^c = C^c x^c \quad (3b)$$

where the system state is $x^c = (\Delta\psi, \delta y, x_{d1}, x_{d2}, T_{\text{dr}}^{\text{ff}}, x_{d3}, x_{d4}, T_{\text{dr}}^{\text{fb}})^T$, the input is $u^c = (\rho, \beta, r, \delta_s)^T$, and the output is $y^c = T_{\text{dr}}^{\text{ff}} + T_{\text{dr}}^{\text{fb}} = T_{\text{dr}}$. In the previous expressions, $T_{\text{dr}}^{\text{ff}}$ and $T_{\text{dr}}^{\text{fb}}$ denote the two components of the driver's steering torque, resulting from the feedforward path and the feedback path of the driver model, respectively. Specially, referring to Fig. 1, $T_{\text{dr}}^{\text{ff}}$ and $T_{\text{dr}}^{\text{fb}}$ can be expressed as follows:

$$T_{\text{dr}}^{\text{ff}} = (T_{\text{com}} + T_{\text{ant}})G_L G_{\text{nm}} \quad (4a)$$

$$T_{\text{dr}}^{\text{fb}} = -\delta_s G_{k_1} (1 + G_{k_2}) G_{\text{nm}}. \quad (4b)$$

By measuring u^c and y^c , we can identify the driver parameter vector p in (3a) and (3b). To this end, we define an alternative parameter vector $\nu = (\nu_1, \nu_1, \dots, \nu_{12})^T$ as follows:

$$\begin{aligned} \nu_1 &= \frac{1}{p_4}, & \nu_2 &= \frac{1}{p_6}, & \nu_3 &= \frac{1}{p_5}, & \nu_4 &= \frac{p_1}{p_5} \\ \nu_5 &= \frac{p_2 p_3}{p_4 p_6 p_7}, & \nu_6 &= \frac{p_2}{p_4 p_7}, & \nu_7 &= p_7, & \nu_8 &= p_8 \\ \nu_9 &= p_9, & \nu_{10} &= \frac{1}{p_{10}}, & \nu_{11} &= p_{11}, & \nu_{12} &= \frac{1}{p_{12}}. \end{aligned} \quad (5)$$

The mathematical expressions in the sequel can be simplified by using ν instead of p . The system matrices in (3a) and (3b) are given explicitly by (6). It is worth mentioning that, V_x is assumed to be constant in (6). One can add V_x to the input vector u^c for varying velocity cases.

Since we are interested in identifying the parameter vector ν , we augment the state with ν and define the new augmented state

$$\left[\begin{array}{c|c} A^c(\nu) & B^c(\nu) \\ \hline C^c & 0 \end{array} \right] = \left[\begin{array}{cccccccc|cccc} 0 & 0 & 0 & 0 & 0 & 0 & 0 & 0 & V_x & 0 & -1 & 0 \\ V_x & 0 & 0 & 0 & 0 & 0 & 0 & 0 & V_x \nu_7 & -V_x & -\nu_7 & 0 \\ 0 & \nu_6 - \frac{\nu_1 \nu_5}{\nu_2} & -\nu_1 & 0 & 0 & 0 & 0 & 0 & 0 & 0 & 0 & 0 \\ 4 \frac{\nu_2 \nu_4}{\nu_3} & 4\nu_5 & 4\nu_2 & -2\nu_2 & 0 & 0 & 0 & 0 & 4 \frac{L_s \nu_2 \nu_4}{\nu_3} & 0 & 0 & 0 \\ -\nu_4 & -\frac{\nu_5 \nu_3}{\nu_2} & -\nu_3 & \nu_3 & -\nu_3 & 0 & 0 & 0 & -L_s \nu_4 & 0 & 0 & 0 \\ 0 & 0 & 0 & 0 & 0 & 0 & 0 & -\nu_3 \nu_{10} \nu_{12} & 0 & 0 & 0 & 0 \\ 0 & 0 & 0 & 0 & 0 & 0 & 1 & 0 & -\nu_3 \nu_{10} & -\nu_3 \nu_{12} & -\nu_{10} \nu_{12} & -\nu_3 \nu_8 \nu_{12} (\nu_9 + 1) \\ 0 & 0 & 0 & 0 & 0 & 0 & 1 & 0 & -\nu_3 & -\nu_{10} & -\nu_{12} & -\nu_3 \nu_8 (\nu_9 \nu_{11} \nu_{12} + 1) \\ \hline 0 & 0 & 0 & 0 & 1 & 0 & 0 & 1 & 0 & 0 & 0 & 0 \end{array} \right]. \quad (6)$$

$x = [(x^c)^T \nu^T]^T$. The augmented-state system is then given by

$$\dot{x} = \begin{bmatrix} A^c(\nu) \\ 0 \end{bmatrix} x + \begin{bmatrix} B^c(\nu) \\ 0 \end{bmatrix} u \quad (7a)$$

$$y = [C^c \ 0] x \quad (7b)$$

where $u = u^c$. Notice that although the system in (3a) and (3b) is linear, the system in (7a) and (7b) is nonlinear, since the matrices A^c and B^c depend on the augmented state x . If we discretize the system in (7a) and (7b), we obtain the following discrete augmented system with additive noise terms

$$x_{k+1} = A_D(\nu)x_k + B_D(\nu)u_k + w_k \quad (8a)$$

$$y_k = C_D x_k + v_k \quad (8b)$$

where w_k and v_k are the process noise and the measure noise, respectively. As usual, these noise terms are included to model neglected/unmodeled uncertainties.

In the following sections, we estimate the state vector of the system in (3a) or (7) based on the available data, subject to the following constraints:

$$p_i \leq g_i(\nu) \leq \bar{p}_i, \quad i = 1, 2, \dots, 12 \quad (9)$$

where $g_i(\nu)$ is the i th element of the vector-valued function $g(\nu)$ given by

$$g(\nu) = [1/\nu_1 \ 1/\nu_2 \ 1/\nu_3 \ \nu_4/\nu_3 \ \nu_5/(\nu_2\nu_6) \\ (\nu_6\nu_7)/\nu_1 \ \nu_7 \ \nu_8 \ \nu_9 \ 1/\nu_{10} \ \nu_{11} \ 1/\nu_{12}]^T. \quad (10)$$

Note that some of the parameters in the feedback model, in particular in the neuromuscular system $G_{nm}(s)$, can be considered to be constants that do not change significantly from driver to driver [9], [39]. These parameters will be discussed in Section VI-A.

III. DRIVER PARAMETER ESTIMATION

In this section, we use a joint EKF/UKF and a dual EKF/UKF to estimate the system states and obtain the unknown driver parameters. The joint EKF/UKF includes the unknown parameters into the original state vector and then estimates the states and the parameters simultaneously. The dual EKF/UKF separates the states and the parameters, so as to estimate the states and the parameters separately.

A. Nonlinear Kalman Filter

The EKF is a classical approach to solve nonlinear estimation problems. This is achieved by means of linearizing the nonlinear state transition and nonlinear observation models. Let the discrete system

$$x_{k+1} = f(x_k, u_k, w_k) \quad (11a)$$

$$y_k = h(x_k, u_k, v_k) \quad (11b)$$

where w_k and v_k are the process noise and the measure noise, respectively, both of which are assumed to be with zero-mean

white Gaussian with covariances given by

$$\mathbb{E}(w_t w_s^T) = Q_w \delta_{ts}, \quad \mathbb{E}(w_t v_s^T) = Q_c \delta_{ts}, \quad \mathbb{E}(v_t v_s^T) = Q_v \delta_{ts} \quad (12)$$

where Q_w , Q_c , and Q_v are the covariance matrices and δ_{ts} is the Kronecker delta function defined by

$$\delta_{ts} = \begin{cases} 1, & \text{if } t = s \\ 0, & \text{if } t \neq s. \end{cases} \quad (13)$$

We assume that w_t and v_s are independent Gaussian random variables and hence the cross term Q_c in (12) is zero. The state estimates can then be computed using the EKF algorithm [34].

An alternative to EKF is to use an UKF. A UKF implements the unscented transform (UT) [32], and avoids calculating the Jacobian matrices at each time step. Hence, it captures the true mean and the covariance of the state Gaussian random variable to at least second-order accuracy for any nonlinearity. Let us consider the system in (11a) and (11b). The UKF redefines the state vector as $x_k^a = [x_k^T, w_k^T, v_k^T]^T$ and estimates x_k^a recursively. The UT sigma point selection scheme is applied to calculate the sigma matrix \mathcal{X}_k^a for the augmented state x_k^a .

Although the UKF-based algorithms (joint/dual UKF) are expected to have better accuracy, the choice between the joint estimation and the dual estimation is still not clear, since they show different performances when they are applying to different problems. More discussions can be found, for instance, in [32], [33].

B. Nonlinear State Constraints

Recall that the parameter vector ν to be estimated is constrained by the nonlinear inequalities in (9). The Kalman filtering constrained state estimation problem has been solved using a number of algorithms [40]–[42]. The available approaches for solving linear equality constraint problems include model reduction [43], perfect measurement [44], estimate projection [40], system projection [45], and soft constraints [46]. The available methods for solving nonlinear equality constraints problems include Taylor expansion approximation [47], smoothly constrained Kalman filter [48], moving horizon estimation [49], unscented Kalman filtering [50], and particle filters [51]. In this study, we use the estimate projection algorithm and the first-order Taylor expansion approximation method to solve the state estimation problem with nonlinear inequality constraints in (9).

Geometrically, the idea is to project the unconstrained estimate $\hat{x}(k)$ onto the constraint surface. Mathematically, we solve the following minimization problem:

$$\tilde{x}_k = \underset{x}{\operatorname{argmin}} \quad (x - \hat{x}_k)^T W (x - \hat{x}_k) \quad (14a)$$

$$\text{such that } g(x) \leq b \quad (14b)$$

where \hat{x}_k and \tilde{x}_k are the unconstrained estimate and the constrained estimate of the state at the time step k , respectively, W is the weighting matrix, and $g: \mathbb{R}^n \rightarrow \mathbb{R}^m$ is a nonlinear vector-valued function. Performing a Taylor series expansion of (14b) around $\hat{x}(k)$, yields

$$g(x) \approx g(\hat{x}_k) + g'(\hat{x}_k)(x - \hat{x}_k) + \dots, \quad (15)$$

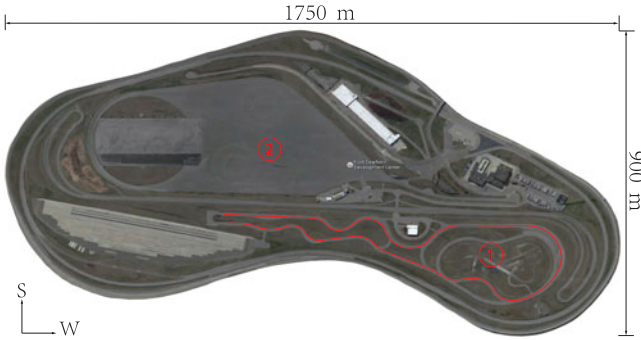


Fig. 3. Proving ground by the Google map.

and after ignoring higher order terms, we obtain a linear approximation of the constraint inequalities in (14b)

$$g'(\hat{x}_k)x \leq b - g(\hat{x}_k) + g'(\hat{x}_k)\hat{x}_k. \quad (16)$$

The minimization problem (14a) subject to the linear inequality constraints in (16) can be solved using standard quadratic programming [11], [52].

IV. FIELD TESTS

Several field tests were conducted to validate the previous driver model. The field tests took place at the Ford Dearborn Proving Ground (DPG) in Michigan during November 2015. The Ford DPG is about 1750 m from West end to East end and about 900 m from South end to North end. The width of the double-lane road is about 6 m. Three kinds of tests were conducted. A steering handling course (SHC) test, a fixed-radius circling (FRC) test, and the public road test (PRT). The SHC and FRC tests were conducted at zone 1 and zone 2 of the proving ground, respectively (see Fig. 3). Three vehicles differing in size and engine power were prepared and were driven by a professional driver mimicking three different types of drivers having distinct driving skills (novice, experienced, and racing). This was done mainly for safety reasons, as untrained novice drivers were not allowed to use the DPG. Consequently, a natural next step along this research direction would be the collection of more data (primarily from untrained novice drivers on the road) in order to further corroborate the conclusions of this paper.

In both the SHC test and the FRC test, the driver was required to maintain the vehicle at a constant velocity throughout the road, while in the PRT test, the driver drove freely on a section of a prechosen public road, considering the specific traffic conditions. The proving ground, the experimental vehicles and the drivers were provided by the Ford Motor Company. Fig. 4 shows the experimental vehicles and the main equipment used for the tests. All data were collected through a controller area network (CAN) analyzer that interconnected the computer and the in-vehicle CAN buses. There are two CAN channels, namely, the HS-CAN and INFO-CAN channel, both of which have a data transfer rate of 500 [kB/s]. The HS-CAN connects to most of the regular on-board electronic control units (ECU), such as the antiskip braking system (ABS), the electric power assisted steering (EPAS) system and the restraints control



Fig. 4. Experiment vehicles and some apparatus. 1st row: Fiesta (left), MKS (medium), F150 (right); second row: power source (left), power converter (medium), CAN case (right).

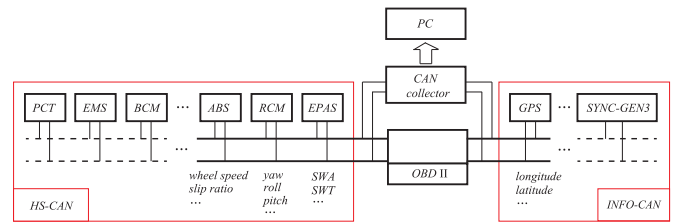


Fig. 5. Illustration of the CAN network on MKS.

TABLE I
SHC (CONSTANT VELOCITY); CW=CLOCKWISE, CCW=COUNTER
CLOCKWISE

SHC	Novice	Experienced	Racing
30 [mph]	1 lane, unsmooth	1 lane, smooth	2 lanes, smooth
45 [mph]	1 lane, unsmooth	1 lane, smooth	2 lanes, smooth
	FRC	R=85 [m]	R=200 [m]
	30 [mph]	CW and CCW	CW and CCW
	45 [mph]	CW and CCW	CW and CCW
	PRT	Novice	Experienced
	Westward	unsmooth	smooth
	Eastward	unsmooth	smooth

module (RCM). These ECUs share the data on the HS-CAN bus. The INFO-CAN connects to the in-vehicle communications and entertainment system—called the SYNC system, which incorporates the global position system (GPS) and the navigation module.

The data collected during the tests were the steering wheel angle, the steering column torque, the yaw rate, and the longitude and the latitude of the vehicle. The signals of the steering wheel angle and the steering column torque were provided by the EPAS, the yaw rate signal was provided by the RCM and position information was provided by the on-board GPS system. Additional variables such as the vehicle yaw angle, the velocity/acceleration of the vehicle, the side slip angle, and the road curvature were estimated based on the yaw rate and the GPS position data. The CAN bus network of the MKS is shown in Fig. 5. The setup of the test conditions for the SHC, FRC, and PRT tests are summarized in Table I.

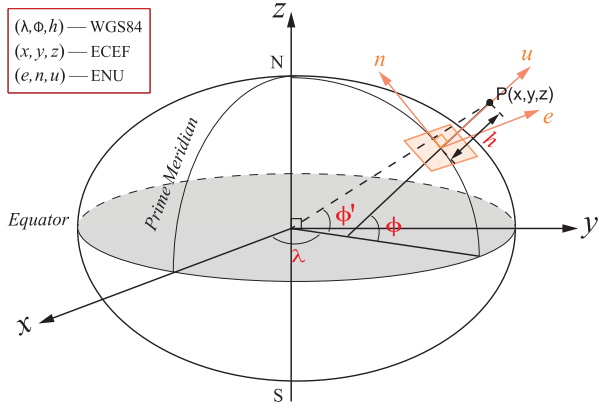


Fig. 6. Illustration on the different coordinate systems.

V. DATA ANALYSIS AND RESULTS

In this section, we summarize the data processing step from the driving tests and we apply the joint EKF/UKF and the dual EKF/UKF to estimate the parameters of the assumed driver model. Based on the data analysis, a refined driver model is proposed to better reproduce the actual steering wheel torque command of the driver.

A. GPS Data Processing

Since the road curvature and the side slip angle of the vehicle were not directly measured, we first obtain the missing values by processing the GPS data, which are given in the form of latitude and longitude. We refer to the method proposed in [53], by which the GPS coordinates are transformed to local navigation coordinates East, North, and Up (ENU) (in this paper, the height is zero since the vehicle is traveling on the ground). Three useful coordinate systems used in this transformation are shown in Fig. 6, namely, the World Geodetic System 1984 (WGS84), the Earth Centered Earth Fixed (ECEF) system and the ENU system. The WGS84 system expresses the position vector in terms of the longitude, the latitude and the height (ϕ, λ, h) of the vehicle, while the ECEF system is in terms of the vehicle Cartesian coordinates (x, y, z) . The ENU system is represented locally, which usually works as the navigation coordinate system.

We first converted the GPS coordinates to ECEF coordinates using the following equations:

$$x = \frac{a \cos \phi \cos \lambda}{\chi}, \quad y = \frac{a \cos \phi \sin \lambda}{\chi}, \quad z = \frac{a(1 - e^2) \sin \phi}{\chi} \quad (17)$$

where $\chi = \sqrt{1 - e^2 \sin^2 \phi}$, $a \approx 6.39 \times 10^6$ [m] and $e^2 \approx 6.69 \times 10^{-3}$ are the semimajor axis and the first numerical eccentricity of the earth, respectively. By performing a Taylor expansion of (17) about ϕ and λ and omitting terms higher than second order, we obtain

We finally rotate the ECEF coordinates to obtain the ENU coordinates using the following equations:

$$\begin{pmatrix} de \\ dn \end{pmatrix} = \begin{pmatrix} -\sin \lambda & \cos \lambda & 0 \\ -\sin \phi \cos \lambda & -\sin \phi \sin \lambda & \cos \phi \end{pmatrix} \begin{pmatrix} dx \\ dy \\ dz \end{pmatrix}. \quad (19)$$

The trajectory of the vehicle can be obtained by integrating the ENU coordinates de and dn in (19). The side slip angle β is estimated using the equation [54]

$$\beta = \arctan\left(\frac{V_y}{V_x}\right) - \psi \quad (20)$$

where V_x and V_y are the longitudinal velocity and the lateral velocity of the mass center of the vehicle chassis, respectively, and ψ is the yaw angle. The road curvature ρ is calculated by

$$\rho = \frac{Y''_{\text{cog}}}{(1 + Y_{\text{cog}}'^2)^{3/2}} \quad (21)$$

where $Y'_{\text{cog}} = \partial Y_{\text{cog}} / \partial X_{\text{cog}}$, $Y''_{\text{cog}} = \partial Y'_{\text{cog}} / \partial X_{\text{cog}}$, and X_{cog} and Y_{cog} are the coordinates of the vehicle in the local ENU system.

B. Driver Parameter Identification

This section shows the results from the previous driver parameter identification and validation procedure, and provides a comparative analysis. Before processing the field test data, we first implemented the identification approach on a set of data obtained from CarSim/MATLAB simulation. This was done in order to confirm the correctness and limitations of the identification algorithm.

1) *CarSim Data Processing*: The vehicle model used in the simulation was configured with CarSim 8.0 [55] and was

$$\begin{aligned} dx &= -\frac{a \cos \lambda \sin \phi (1 - e^2)}{\chi^3} d\phi - \frac{a \sin \lambda \cos \phi}{\chi} d\lambda + \frac{1}{4} a \cos \phi \cos \lambda (-2 \\ &\quad - 7e^2 + 9e^2 \cos^2 \phi) d\phi^2 - \frac{a \sin \lambda \sin \phi (1 - e^2)}{\chi^3} d\phi d\lambda - \frac{a \cos \lambda \cos \phi}{2\chi} d\lambda^2 \\ dy &= -\frac{a \sin \lambda \sin \phi (1 - e^2)}{\chi^3} d\phi + \frac{a \cos \lambda \cos \phi}{\chi} d\lambda + \frac{1}{4} a \cos \phi \sin \lambda (-2 \\ &\quad - 7e^2 + 9e^2 \cos^2 \phi) d\phi^2 - \frac{a \cos \lambda \sin \phi (1 - e^2)}{\chi^3} d\phi d\lambda - \frac{a \sin \lambda \cos \phi}{2\chi} d\lambda^2 \\ dz &= \frac{a \cos \phi (1 - e^2)}{\chi^3} d\phi + \frac{1}{4} a \sin \phi (-2 - e^2 + 9e^2 \cos^2 \phi) d\phi^2. \end{aligned} \quad (18)$$

TABLE II
CONSTANT PARAMETERS OF THE SYSTEM

m	Mass of vehicle	1653	kg
ℓ_f	Distance from center of gravity to front axis	1.402	m
ℓ_r	Distance from center of gravity to rear axis	1.646	m
L_s	Distance from center of gravity to far-field visual point	15	m
I_z	Moment of inertia of the vehicle	2765	kgm ²
J_s	Moment of inertia of the steering column	0.11	kgm ²

TABLE III
DRIVER MODEL PARAMETERS; JEKF=JOINT EKF, DEKF=DUAL EKF,
UB=UPPER BOUND, LB=LOWER BOUND

Parameter	JEKF ₃	JEKF	JUKF	DEKF	DUKF	UB	LB
K_a [Nm]	56.56	22.10	21.62	21.29	21.29	100	5
K_c [Nm]	19.82	149.87	152.35	151.88	150.96	200	5
T_L [s]	0.90	0.33	0.34	0.33	0.33	5	0
T_I [s]	0.48	0.26	0.26	0.26	0.26	0.5	0
T_N [s]	0.30	0.18	0.19	0.19	0.20	0.3	0.01
t_p [s]	0.19	0.11	0.11	0.11	0.11	0.5	0.01
ℓ_s [m]	3.47	12.06	12.16	12.25	12.07	15	3
K_D [Nm]	1.50	0.37	0.27	0.11	0.31	1.5	0.1
K_G	-0.41	-0.74	-0.64	-0.79	-0.43	-0.4	-1.5
T_{k1} [sec]	1.05	1.50	1.54	1.97	1.57	6	1
T_{k2} [sec]	5.13	3.82	3.71	3.42	3.81	6	1
T_{k3} [sec]	0.01	0.01	0.01	0.01	0.01	0.03	0.01

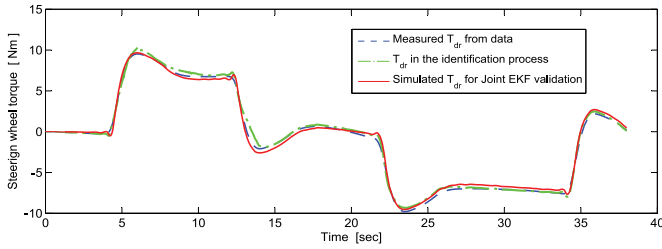


Fig. 7. Data, the training curve, and the simulated curve for the steering wheel torque.

initialized with a constant speed of 15 [m/s] (54 [km/h]). Other vehicle constants can be found in Table II. In addition, we assumed a high-adhesion asphalt pavement with a constant friction factor of 0.89 for all simulations. The length and the width of the road were configured as 1000 [m] and 6 [m], respectively. A path composed of a sequence of straight segments, circular segments, and clothoids was given as an input. The configured road curvature was obtained through a sensor provided by CarSim. Since the road curvature data from CarSim are noisy, we applied a first-order lowpass filter with a cutoff frequency at 2.5 rad/s to eliminate the noise before inputting this signal to the driver model.

After collecting the necessary simulation data, namely, the steering wheel angle δ_s , the road curvature ρ , the side slip angle β , and the yaw rate r in the input vector u^c , and the steering wheel torque T_{dr} in the output y^c . We then implemented the joint EKF to estimate the driver model parameters. The results are given in Fig. 7. We only show the results of the joint EKF here, since the results given by the other filters were quite similar. In Fig. 7, the blue dashed curve shows the steering wheel torque

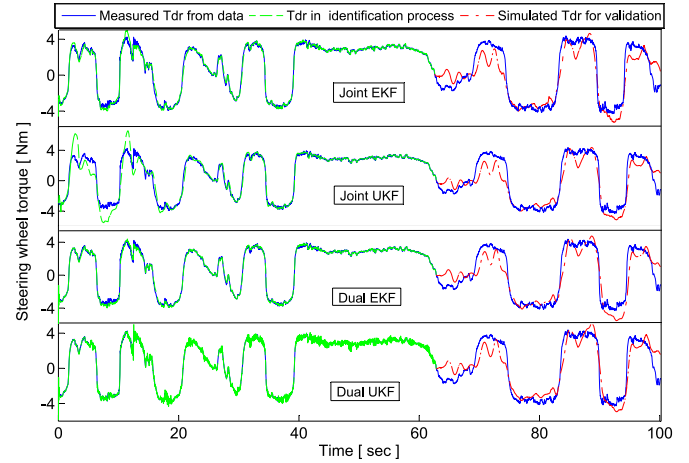


Fig. 8. Data, the training curve, and the simulated curve from the Joint/Dual E-/UKF.

from the data, the green dot-dash curve shows the estimation of the steering wheel torque during the training process, and the red solid curve shows the validation result, which is obtained by using the identified driver model parameters from the training process in the simulation. The simulated result agrees well with the data. The identified driver model parameters are given in the second column of Table III.

2) *Field Test Data Processing*: We processed the field test data using the joint EKF, the joint UKF, the dual EKF, and the dual UKF separately, so that we can compare the identified driver parameters obtained from these four different methods. For instance, we took the set of data from the SHC tests corresponding to the conditions of a “Racing Driver” with a constant velocity of 45 [mph] in Table I. In each implementation, we used the first 60% of the data for parameter training and then used the remaining 40% of the data for validation.

By designing the appropriate Kalman filter parameters, such as the process noise covariance, the measurement noise covariance, and the initial state covariance matrix, we obtained reasonably good estimation of the parameters. The process noise covariance is considered to be the most critical, and therefore had to be carefully tuned [56], [57]. Fig. 8 illustrates the steering wheel torque from data, the training curve for each filter, and the simulated output corresponding to the identified model parameters. The green dashed plots in Fig. 8 show how the prediction of the steering wheel torque at the current time step, provided by the joint/dual E-/UKF based on past data, agrees with the current data. After about 1 min the prediction results get stabilized and agree well with the data.

The trajectories of the estimated states (we only show the driver parameters, and each parameter is scaled such that the initial value is one) corresponding to the joint EKF are given in Fig. 9. The red dash-dot plots in Fig. 8, which are drawn to validate the identified driver parameters, agree well with the data. Although one sees some difference between the validation results and the data, the results are reasonable, since the parameters of the real driver may change slowly with time. This effect is investigated next.

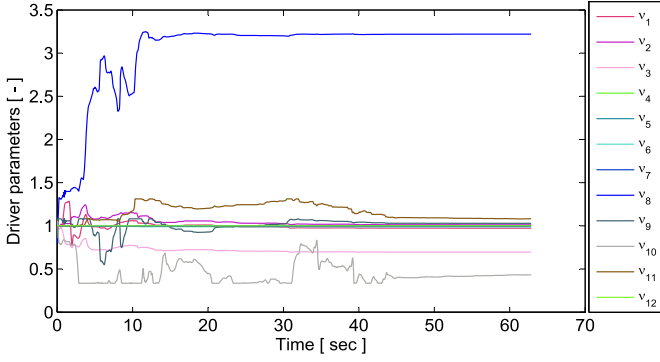


Fig. 9. Time histories of the driver parameters during the training process. Steady state is reached after 45 s.

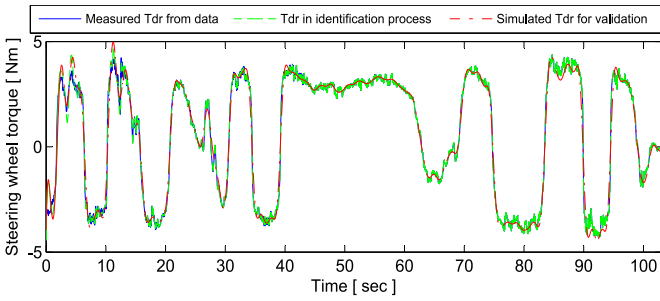


Fig. 10. Data, the training curve, and the simulated curve from the Joint UKF.

C. Driver Model Refinement

Based on the results from the previous section, we refined the model by assuming that the process noise for the parameter vector ν is colored. To this end, we let

$$\dot{\nu} = \zeta, \quad \dot{\zeta} = \xi \quad (22)$$

where ξ is a zero-mean white process noise and ζ is a colored process noise with unknown time-varying mean. By discretizing (22) with a sampling interval Δt , one obtains

$$\nu_k = \nu_{k-1} + \Delta t \zeta_{k-1}, \quad \zeta_k = \zeta_{k-1} + \Delta t \xi_{k-1}. \quad (23)$$

If ξ_{k-1} is uncorrelated with ζ_{k-1} , ζ_k is colored process noise in the sense that ζ_k is correlated with itself at different time steps [58]

$$\mathbb{E}(\zeta_k \zeta_{k-1}^T) = \mathbb{E}(\zeta_{k-1} \zeta_{k-1}^T + \Delta t \xi_{k-1} \zeta_{k-1}^T) = \mathbb{E}(\zeta_{k-1} \zeta_{k-1}^T) \triangleq Q_\zeta \quad (24)$$

where $Q_\zeta \neq 0$ is the covariance matrix. For the noise ζ at any two different time steps t and s ($t > s$) one obtains that $\mathbb{E}(\zeta_t \zeta_s^T) = \mathbb{E}(\zeta_{t-1} \zeta_s^T) = \dots = \mathbb{E}(\zeta_s \zeta_s^T) = Q_\zeta$, and hence one can summarize the covariances for ζ and ξ as follows:

$$\mathbb{E}(\zeta_t \zeta_s^T) = Q_\zeta, \quad \mathbb{E}(\zeta_t \xi_s^T) = 0, \quad \mathbb{E}(\xi_t \xi_s^T) = Q_\xi \delta_{ts} \quad (25)$$

where Q_ξ is the covariance matrix and δ_{ts} is given by (13).

Equations (22) allow the parameter vector ν to drift with time. We implemented all filters using this model and recorded the estimates of ν at each time step. We then performed simulations with the time-varying parameters. Fig. 10 shows the results for the Joint UKF case. The results with the other filters are similar,

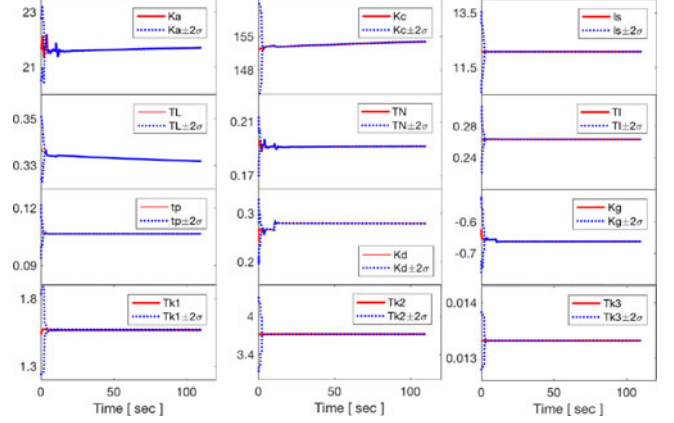


Fig. 11. Trajectory of the driver parameters with $\pm 2\sigma$ error during the training process.

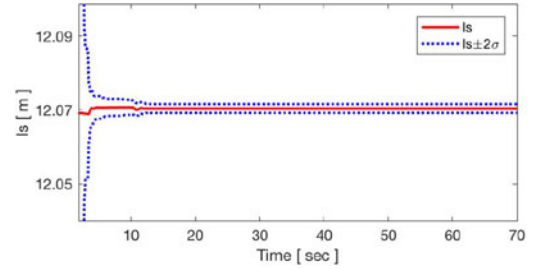


Fig. 12. Detail of estimate of ℓ_s along with the 2σ confidence bounds.

and are thus, omitted. Fig. 10 indicates that the parameterized driver model with time-varying parameters characterizes the driver's steering behavior much more accurately. This implies that the parameterized two-point visual driver model architecture shown in Fig. 1 is valid, but the parameters are not necessarily constant, and may vary slowly with time. The driver parameters convergence with time, along with their 2σ -bounds, are shown in Fig. 11. Fig. 12 shows in greater detail the estimate (solid red line) and the confidence levels (blue dotted line) for ℓ_s . The plots for the other parameters are similar. From Fig. 11 one observes that, although most of the parameters converge to some constants, some of them exhibit drift, specifically, K_a , K_c , and T_L . This behavior accounts for the difference between the simulation result (red line) and the test data (blue line) shown in Fig. 8. In terms of driver parameter identification, this result suggests that K_a , K_c , and T_L are the most important parameters to track in an online identification scheme.

VI. DRIVER COMPARISON AND ANALYSIS

Section V estimates the identified driver parameters using four different nonlinear filters. Our main motivation for parameter estimation is to be able to distinguish the different driver styles based on the identified driver parameters from experimental data. Empirical evidence suggests that one potential strong distinguishing feature of driver style is the smoothness of the applied steering command [59], [60]. In order to test this theory, we first analyzed the driver's steering behavior according to the identified driver parameters, and we then analyzed the

TABLE IV
DRIVER MODEL PARAMETERS

Parameter		K_a	K_c	T_L	T_1	T_N	t_p	ℓ_s	K_D	K_g	T_{k_1}	T_{k_2}	T_{k_3}
30 mph	Racing	21.7	153.5	0.33	0.26	0.19	0.11	12.1	0.28	-0.66	1.57	3.72	0.013
	Experienced	21.9	158.6	0.35	0.28	0.20	0.11	12.1	0.66	-0.40	5.95	3.73	0.013
	Novice	17.1	113.5	0.25	0.20	0.15	0.10	8.7	0.37	-0.40	2.92	3.29	0.013
45 mph	Racing	21.9	155.8	0.33	0.26	0.19	0.11	12.1	0.30	-0.66	1.53	3.72	0.013
	Experienced	21.8	156.8	0.35	0.28	0.19	0.11	12.2	0.35	-0.78	2.31	3.73	0.013
	Novice	17.4	121.4	0.27	0.21	0.16	0.08	8.8	0.33	-0.81	5.65	3.21	0.013

driver's steering behavior by comparing the wavelet transform of the control signals from different drivers, since it is well-known that wavelet transform contains information about the local smoothness of a signal [61].

A. Driver Parameter Analysis

Table IV shows the parameters for the racing, experienced and novice driver in the SHC tests (MKS vehicle). Since some of the parameters are varying with time (namely, K_a , K_c , and T_L), we only show their time-average values in Table IV.

From the tests shown in Table IV, one observes that K_c is much larger than K_a . This indicates that in the lane-keeping task the driver pays more attention to θ_{near} than θ_{far} , as expected. This result may change, however, for a different driving task [22]. In this section, we wish to compare the experienced driver steering command with the novice driver steering command for the same task. The question we wish to answer is whether we are able to distinguish between these two (supposedly) distinct driver styles by analyzing only the driver steering command. From Table IV, one sees that the parameters K_a , K_c , T_L , and T_1 for the novice driver are smaller than that for the experienced driver. The anticipatory gain K_a and the compensatory gain K_c represent the attention the driver pays to θ_{far} and θ_{near} , respectively. An increase of K_a leads to $d\theta_{\text{far}}/dt < 0$ (oversteering), and the vehicle gets closer to the inner curb of the road. An increase of K_c leads to more compensation ($d\theta_{\text{near}}/dt < 0$), and the vehicle gets closer to the road centerline. Saleh *et al.* [30] mentioned that K_c may depend on the driver's cautiousness (e.g., the driver avoids driving too close to the border line) and small K_c leads to a great tendency to cut around the bends. The parameters T_L and T_1 define a lead compensation in the compensatory control path of the driver. A larger T_L corresponds to higher compensation rate of θ_{near} (the speed of θ_{near} to reach the desired value), but the system will be oscillating if T_L is too large [30]. T_1 determines the bandwidth of the frequencies of θ_{near} to be compensated. Small values of T_1 mean that the driver compensates all frequencies including the high-frequency noise, hence leading to an oscillatory system. If T_1 is large ($T_1 < T_L$), the bandwidth of the compensatory loop is narrow such that most frequencies of θ_{near} are filtered.

The Bode plots of the lead compensator G_c are shown in Fig. 13. One sees that the magnitude of G_c for the novice driver is the smallest and the center frequency is the highest. This indicates that the compensatory control of the novice driver is slow and the driver is more likely to compensate the high fre-

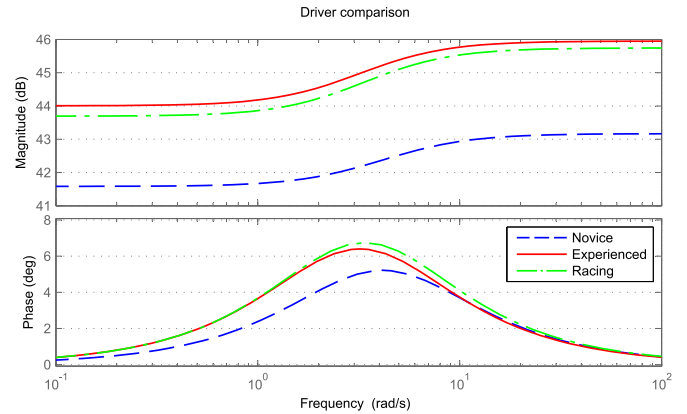


Fig. 13. Bode plots of G_c for the novice, the experienced and the racing drivers, 45 mph.

quencies of θ_{near} . The near field of view visual distance ℓ_s for the novice driver in Table IV is smaller than that for the experienced and the racing drivers. This does not necessarily imply, however, that the larger the preview distance ℓ_s the better. For instance, Damveld and Happee [62] observed that the driver's compensatory behavior is reduced with increasing preview distance (5–100 [m]) and pointed out that, with a preview distance above a certain point, the drivers no longer minimize the lateral error but use the additional preview to obtain a smooth path. The preview distance may also depend on the road geometry [63].

We analyzed the high-frequency feedback part $G_{fb} = G_{k1}(1 + G_{k2})$ of the model (see Fig. 1), where G_{k1} and G_{k2} are given by (1). The Bode plots for the three drivers using the identified parameters are shown in Fig. 14. Fig. 14 shows that G_{fb} has phase lead and high pass properties, and the three Bode plots look quite close to each other. Considering that the input signal to G_{fb} (steering wheel angle) typically does not have many high-frequency components, and the low frequencies are filtered, only a narrow band of frequencies can effectively pass through G_{fb} as feedback to the driver. This result indicates that the effect of the high-frequency feedback may be small, and hence the visual information is more important to the driver than the steering feel in his/her hands during a lane-keeping task. Fig. 14 also indicates that the parameters in G_{fb} do not distinguish between the drivers since the Bode plots are close to each other. We may thus be able to fix the parameters in G_{fb} to represent the steering behaviors of different drivers, as in [9], [22], where K_D and T_{k1} are considered to be constants (i.e., $K_D = 1$, $T_{k1} = 2.5$). It is worth mentioning that, besides

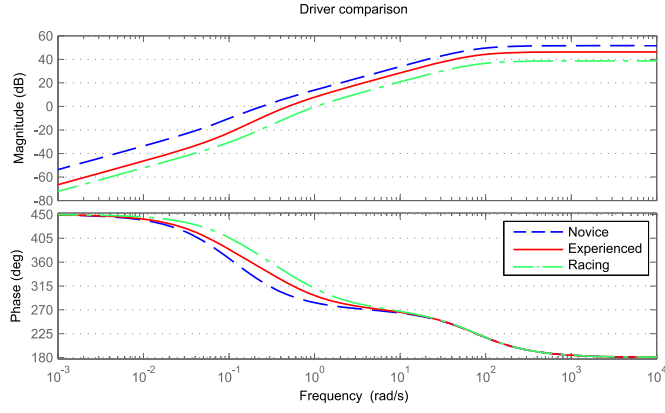


Fig. 14. Bode plots of G_{fb} for the novice, the experienced and the racing drivers (45 mph).

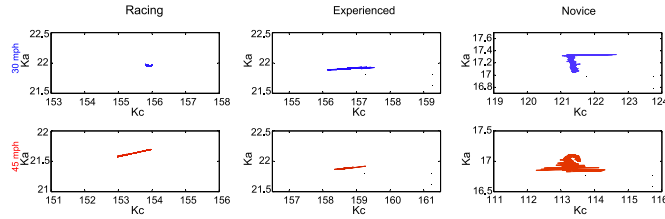


Fig. 15. Plots of K_a versus K_c for the three types of drivers.

K_D and T_{k_1} in [9], [22], the time delay t_p and the parameter T_N in the neuromuscular system are also treated as constants (i.e., $t_p = 0.151$, $T_N = 0.11$).

Fig. 15 shows the plots of K_a versus K_c . As shown from the analysis of the experimental data in Section V-C, the gains K_a and K_c drift with time. Furthermore, the parameters of the novice driver change faster and take values in a larger range than both the experienced driver and the racing driver. This result may indicate that, at least for a lane-keeping task, the steering behavior of the experienced driver and the racing driver is smoother than the novice driver. To confirm this conjecture, in Section VI-B we perform a wavelet analysis of the control signals of the experienced/racing driver and the novice driver and compare the two.

B. Wavelet Analysis of Driver Steering Torque Command

In this section, we compare the steering commands of the novice, experienced and racing drivers in terms of their frequency characteristics, and local smoothness properties. Recall that the continuous wavelet transform (CWT) for a given signal f at scale $s \geq 0$ and translation $\tau \in \mathbb{R}$ is written as [64], [65]

$$Wf(s, \tau) = \frac{1}{\sqrt{s}} \int_{-\infty}^{+\infty} f(t) \psi^* \left(\frac{t - \tau}{s} \right) dt \quad (26)$$

where ψ^* is the complex conjugate of the mother wavelet ψ . Many available wavelet bases can be used, such as Morlet, Paul, Haar, Daubechies, Coiflets, and Symlets [66], [67].

Fig. 16 shows the steering wheel torques for the novice, experienced and racing driver, respectively. In order to compare the frequency content of the signals, we performed a CWT of the

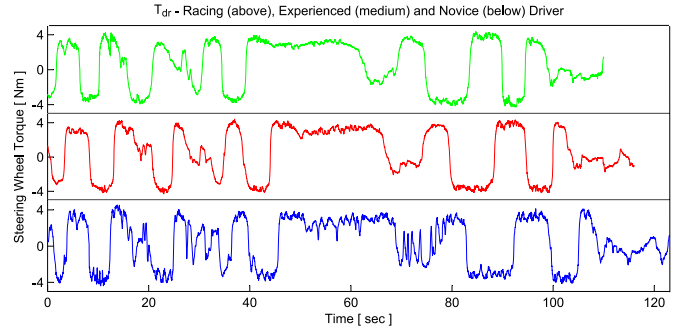


Fig. 16. Steering wheel torque of the racing, experienced and novice driver (MKS, 45 mph).

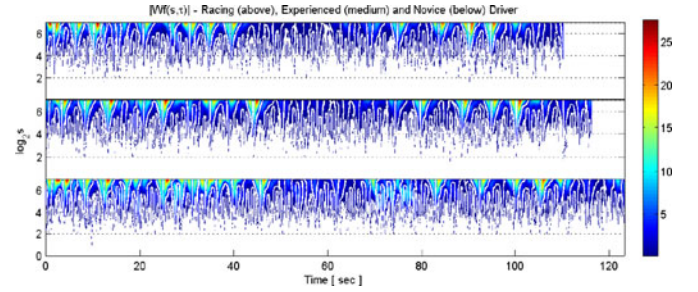


Fig. 17. Wavelet transform of T_{dr} of the racing (above), experienced (medium) and novice (below) driver.

steering wheel torques shown in Fig. 16 using the real-valued Daubechies wavelet 3 function with respect to (26). The graphs of the absolute coefficients of the CWT of the steering wheel torques in Fig. 16 are shown in Fig. 17. The color regions of the graph indicate the local modulus maxima. The results in Fig. 17 show that, in the same SHC, the CWT of the control signal of the novice driver has more local maxima than the experienced and the racing driver. This may be used to evaluate the performance of the steering behavior of the driver. The local maxima can be used to detect the position of the local singularities, as well as to determine the associated Lipschitz exponents using the following theorem [61].

Theorem 6.1: Suppose that the wavelet $\psi(t)$ is the n th derivative of a smooth function, is n times continuously differentiable, and has compact support. Let $f(t)$ be a tempered distribution whose wavelet transform is well defined over $[a, b]$, and let $\tau_0 \in [a, b]$. Assume that there exists $s_0 > 0$ and a constant C , such that for all $\tau \in [a, b]$ and $s < s_0$, the modulus maxima of $Wf(s, \tau)$ belong to the cone defined by

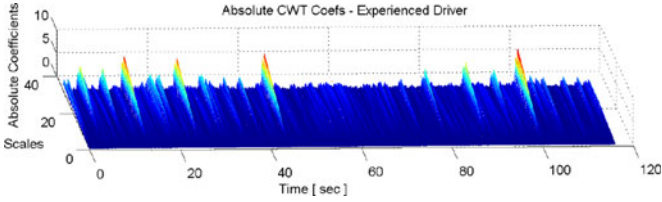
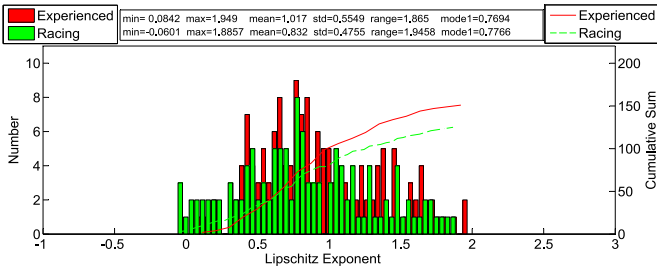
$$|\tau - \tau_0| \leq Cs. \quad (27)$$

Then $f(t)$ is uniformly Lipschitz n in a neighborhood of τ , for all $\tau \in [a, b]$, $\tau \neq \tau_0$. Furthermore, $f(t)$ is Lipschitz α ($\alpha < n$) at τ_0 , if and only if there exists a constant A such that at each modulus maximum (s, τ) in the cone (27)

$$|Wf(s, \tau)| \leq As^\alpha. \quad (28)$$

By taking the logarithm of both sides of (28), one obtains

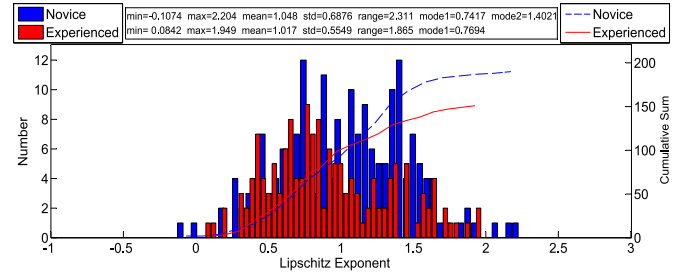
$$\log |Wf(s, \tau)| \leq \log A + \alpha \log s. \quad (29)$$

Fig. 18. Absolute CWT coefficients $|Wf(s, \tau)|$.Fig. 19. Histogram of the Lipschitz exponents α for the experienced and racing driver.

The Lipschitz exponent α is therefore determined by the maximum slope of $\log |Wf(s, \tau)|$ on a logarithmic scale. Here, we only perform CWT of the steering wheel torque of the experienced driver and show the process to determine the Lipschitz exponent. We adopt the Daubechies wavelet 3 that is orthogonal, compactly supported and has three vanishing moments, by which we can determine Lipschitz exponents $\alpha < 3$. Fig. 18 plots the absolute CWT coefficients in the time-scale domain.

We find the lines of maxima from Fig. 18 and determine the positions of the singularities. The singularities are all the points on the time axis that the lines of maxima converge to. There may be multiple lines of maxima converging to the points that are close to each other, due to the number of the vanishing moments of the mother wavelet or the Lipschitz exponent of the singularity [61].

Fig. 19 illustrates the histogram showing the distribution of the Lipschitz exponents corresponding to the experienced and racing driver. By comparing the results in Fig. 19, one observes that the control signal (T_{dr}) of the racing driver has a smaller number of singularities. This result indicates that the steering wheel torque command of the racing driver is smoother than the experienced driver. The distribution of the Lipschitz exponent α of the racing driver shows a smaller minimal, maximal, and mean value than the experienced driver. This statistical result indicates that the singularities of the steering wheel torque command of the racing driver are likely to be more irregular and impulsive than the experienced driver. The racing driver perhaps tends to sacrifice smoothness locally (smaller Lipschitz exponents) by making good use of the double-lane road, such that (s)he could obtain overall better smoothness (fewer singularities) than the experienced driver. The experienced driver, who was only allowed to drive within a single lane of the road, behaved less aggressively since the mean and minimal value of the Lipschitz exponents are larger than the racing driver. Fig. 20 illustrates the histogram showing the distribution of the

Fig. 20. Histogram of the Lipschitz exponents α for the novice and experienced driver.

Lipschitz exponents corresponding to the novice driver and the experienced driver. By comparing the results in Fig. 20, one observes that the control signal (T_{dr}) of the novice driver has a larger number of singularities, and the Lipschitz exponent α shows a larger range from -0.1074 to 2.204 , with a larger standard deviation of 0.6876 . This result implies that the steering wheel torque command of the novice driver is more noisy than the experienced driver (see Fig. 16). Furthermore, the distribution of α exhibits multiple modes, and the first mode on the left is smaller than that of the experienced driver. These features observed from the distribution of the Lipschitz exponents may be used to distinguish the control signals of different drivers and hence classify drivers into different groups.

VII. CONCLUSION

This paper adopts the parameterized two-point visual driver model to characterize the steering behavior of a driver, and conducts a series of field tests to investigate the validity of this model to predict human driver behavior and driving style. We have implemented four nonlinear filters, namely, the joint EKF, the joint UKF, the dual EKF, and the dual UKF to estimate the parameters based on field test data conducted at Ford's Dearborn Development Center test facility. The validation results agree well with the data. The UKF is considered to be more accurate than the EKF in propagating the Gaussian random variables, but the difference is not obvious in this paper. The results of our investigation indicate that some of the driver parameters are not exactly constant, but rather vary slowly during a driving task more than a few minutes long. This observation suggests that similar parameterized driver models need to incorporate this effect to faithfully represent reality.

The main difficulty with the use of the two-point visual driver model in practice is the difficulty of reliably measuring the two visual angles θ_{near} and θ_{far} . In this paper, the road curvature ρ_{ref} is calculated using the GPS data along with the linear estimator in (2) to obtain the values of θ_{near} and θ_{far} . In general, one will need to estimate ρ_{ref} if it is not readily available [37].

The parameters of the driver model provide some interesting features to better understand the steering behavior of different types of drivers. An experienced driver is likely to pay more attention to both the anticipatory control (θ_{far}) and the compensatory control (θ_{near}) than a novice driver. The model parameters may also depend on the driving task [22]. The wavelet transform provides insights into the driver's control signal, in

terms of the number and the location of the singularities of the signal and the distribution characteristics of the associated Lipschitz exponents. These can be used to characterize the control signal into different levels of smoothness. Our analysis showed that the steering wheel torque of an experienced driver has fewer singularities, and the Lipschitz exponents seem to follow a comparatively more concentrated distribution. Based on the work of this paper, a potential next step would be to use machine learning ideas to distinguish the behaviors of the drivers, and to classify the drivers into distinct categories based on features arising from the wavelet transform.

ACKNOWLEDGMENT

The authors would like to thank Mr. D. Starr from Ford Motor Company for the excellent work done in the field test.

REFERENCES

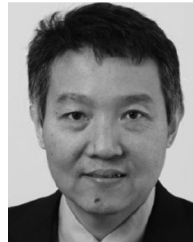
- [1] National Highway Traffic Safety Administration, "Traffic safety facts 2014: A compilation of motor vehicle crash data from the fatality analysis reporting system and the general estimates system," Dept. Transp., Nat. Highway Traffic Safety Adm., Washington, DC, USA, Tech. Rep. DOT-HS-812-261, 2015.
- [2] NHTSA *et al.*, "2015 motor vehicle crashes: Overview," *Traffic Safety Facts Res. Note*, vol. 2016, pp. 1–9, 2016.
- [3] D. Hendricks, J. Fell, and M. Freedman, "The relative frequency of unsafe driving acts in serious traffic crashes," Veridian Engineering, Inc., Buffalo, NY, USA, Rep. DOT-HS-809–206, 2001.
- [4] W. G. Najm, M. D. Stearns, H. Howarth, J. Koopmann, and J. Hitz, "Evaluation of an automotive rear-end collision avoidance system," Dept. Transp., Nat. Highway Traffic Safety Admin., Washington, DC, USA, Tech. Rep. DOT-HS-810-569, 2006.
- [5] G. Li, S. E. Li, and B. Cheng, "Field operational test of advanced driver assistance systems in typical Chinese road conditions: The influence of driver gender, age and aggression," *Int. J. Autom. Technol.*, vol. 16, no. 5, pp. 739–750, 2015.
- [6] D. H. Weir and D. T. McRuer, "Measurement and interpretation of driver steering behavior and performance," SAE Int., Warrendale, PA, USA, SAE Tech. Paper 730098, Feb. 1973.
- [7] C. C. MacAdam, "An optimal preview control for linear systems," *J. Dyn. Syst. Meas. Control*, vol. 102, no. 3, pp. 188–190, 1980.
- [8] C. C. MacAdam, "Application of an optimal preview control for simulation of closed-loop automobile driving," *IEEE Trans. Syst. Man Cybern.*, vol. 11, no. 6, pp. 393–399, Jun. 1981.
- [9] R. Hess and A. Modjtahedzadeh, "A control theoretic model of driver steering behavior," *IEEE Control Syst. Mag.*, vol. 10, no. 5, pp. 3–8, 1990.
- [10] A. Modjtahedzadeh and R. Hess, "A model of driver steering control behavior for use in assessing vehicle handling qualities," *J. Dyn. Syst. Meas. Control*, vol. 115, no. 3, pp. 456–464, 1993.
- [11] A. Burgett and R. Miller, "Using parameter optimization to characterize driver's performance in rear end driving scenarios," in *Proc., Int. Tech. Conf. Enhanc. Safety Veh.*, vol. 2003 May 19–22, 2003, p. 21.
- [12] C. Chatzikomis and K. Spentzas, "A path-following driver model with longitudinal and lateral control of vehicle's motion," *Forsch. Ingenieurwesen*, vol. 73, no. 4, p. 257, 2009.
- [13] D. J. Cole, A. J. Pick, and A. M. C. Odhams, "Predictive and linear quadratic methods for potential application to modelling driver steering control," *Veh. Syst. Dyn.*, vol. 44, no. 3, pp. 259–284, 2006.
- [14] S. D. Keen and D. J. Cole, "Application of time-variant predictive control to modelling driver steering skill," *Veh. Syst. Dyn.*, vol. 49, no. 4, pp. 527–559, 2011.
- [15] M. Flad, C. Trautmann, G. Diehm, and S. Hohmann, "Individual driver modeling via optimal selection of steering primitives," in *Proc. World Congr.*, Cape Town, South Africa, August 24–29, 2014, vol. 19, no. 1, pp. 6276–6282.
- [16] I. Kageyama and H. Pacejka, "On a new driver model with fuzzy control," *Veh. Syst. Dyn.*, vol. 20, no. sup1, pp. 314–324, 1992.
- [17] Y. Lin, P. Tang, W. Zhang, and Q. Yu, "Artificial neural network modelling of driver handling behaviour in a driver-vehicle-environment system," *Int. J. Veh. Des.*, vol. 37, no. 1, pp. 24–45, 2005.
- [18] R. Hamada *et al.*, "Modeling and prediction of driving behaviors using a nonparametric Bayesian method with AR models," *IEEE Trans. Intell. Veh.*, vol. 1, no. 2, pp. 131–138, Jun. 2016.
- [19] C. W. De Silva, *Modeling and Control of Engineering Systems*. Boca Raton, FL, USA: CRC Press, 2009.
- [20] D. L. Wilson and R. A. Scott, "Parameter determination for a Crossover driver model," Dept Mech. Eng. Appl. Mech., Univ. Michigan, Ann Arbor, MI, US, Tech. Rep. UM-MEAM-83–17, 1983.
- [21] L. Saleh, P. Chevrel, F. Claveau, J.-F. Lafay, and F. Mars, "Shared steering control between a driver and an automation: Stability in the presence of driver behavior uncertainty," *IEEE Trans. Intell. Transp. Syst.*, vol. 14, no. 2, pp. 974–983, 2013.
- [22] C. Sentouh, P. Chevrel, F. Mars, and F. Claveau, "A sensorimotor driver model for steering control," in *Proc. IEEE Int. Conf. Syst. Man Cybern.*, San Antonio, TX, USA, October 11–14, 2009, pp. 2462–2467.
- [23] D. D. Salvucci and R. Gray, "A two-point visual control model of steering," *Perception*, vol. 33, no. 10, pp. 1233–1248, 2004.
- [24] J. Steen, H. J. Damveld, R. Happee, M. M. van Paassen, and M. Mulder, "A review of visual driver models for system identification purposes," in *Proc. IEEE Int. Conf. Syst. Man Cybern.*, Anchorage, AK, USA, Oct. 9–12, 2011, pp. 2093–2100.
- [25] E. Donges, "A two-level model of driver steering behavior," *Human Factors*, vol. 20, no. 6, pp. 691–707, 1978.
- [26] M. F. Land and D. N. Lee, "Where do we look when we steer," *Nature*, vol. 369, no. 6483, pp. 742–744, 1994.
- [27] M. F. Land, "The visual control of steering," *Vis. Action*, pp. 163–180, 1998.
- [28] H. Neumann and B. Deml, "The two-point visual control model of steering – new empirical evidence," in *Digital Human Modeling*. Berlin, Germany: Springer, 2011, pp. 493–502.
- [29] G. Markkula, O. Benderius, and M. Wahde, "Comparing and validating models of driver steering behaviour in collision avoidance and vehicle stabilisation," *Veh. Syst. Dyn.*, vol. 52, no. 12, pp. 1658–1680, 2014.
- [30] L. Saleh *et al.*, "Human-like cybernetic driver model for lane keeping," in *Proc. 18th World Congr. Int. Fed. Autom. Control*, Milano, Italy, Aug. 28–Sep. 2, 2011, pp. 4368–4373.
- [31] F. Mars, L. Saleh, P. Chevrel, F. Claveau, and J.-F. Lafay, "Modeling the visual and motor control of steering with an eye to shared-control automation," in *Proc. Human Factors Ergonom. Soc. Annu. Meet.*, vol. 55, no. 1, Las Vegas, NV, USA, Sep. 19–23, 2011, pp. 1422–1426.
- [32] E. A. Wan and R. Van Der Merwe, "The unscented Kalman filter for nonlinear estimation," in *Proc. Adapt. Syst. Signal Process. Commun. Control Symp.*, October 1–4, 2000, pp. 153–158.
- [33] A. Farina, B. Ristic, and D. Benvenuti, "Tracking a ballistic target: Comparison of several nonlinear filters," *IEEE Trans. Aerosp. Electron. Syst.*, vol. 38, no. 3, pp. 854–867, Jul. 2002.
- [34] G. Chowdhary and R. Jategaonkar, "Aerodynamic parameter estimation from flight data applying extended and unscented Kalman filter," *Aerosp. Sci. Technol.*, vol. 14, no. 2, pp. 106–117, 2010.
- [35] S. Noth, I. Rañó, and G. Schöner, "Investigating human lane keeping through a simulated driver," in *Proc. Driver Simul. Conf.*, Paris, France, Sep. 6–7, 2012, pp. 340–345.
- [36] I. Rañó, H. Edelbrunner, and G. Schöner, "Naturalistic lane-keeping based on human driver data," in *Proc. Intell. Veh. Symp.*, Gold Coast, QLD, Australia, Jun. 23–26, 2013, pp. 340–345.
- [37] C. Sentouh, B. Soualmi, J. C. Popieul, and S. Debernard, "Cooperative steering assist control system," in *Proc. IEEE Int. Conf. Syst. Man Cybern.*, Manchester, U.K., Oct. 13–16, 2013, pp. 941–946.
- [38] S. Zafeiropoulos and P. Tsiotras, "Design of a lane-tracking driver steering assist system and its interaction with a two-point visual driver model," in *Proc. Amer. Control Conf.*, Portland, OR, USA, Jun. 4–6, 2014, pp. 3911–3917.
- [39] D. T. McRuer, "Human pilot dynamics in compensatory systems," DTIC Document, Wright Air Development Center, Air Research Development Command, United States Air Force, Wright/Patterson Air Force Base, Dayton, OH, USA, Tech. Rep. AFFDL-TR-65-15, Jul. 1965.
- [40] D. Simon and T. L. Chia, "Kalman filtering with state equality constraints," *IEEE Trans. Aerosp. Electron. Syst.*, vol. 38, no. 1, pp. 128–136, Jan. 2002.
- [41] N. Gupta and R. Hauser, "Kalman filtering with equality and inequality state constraints," Oxford University Computing Laboratory, University of Oxford, 2007. arXiv:0709.2791.

- [42] D. Simon, "Kalman filtering with state constraints: A survey of linear and nonlinear algorithms," *IET Control Theory Appl.*, vol. 4, no. 8, pp. 1303–1318, 2010.
- [43] W. Wen and H. F. Durrant-Whyte, "Model-based multi-sensor data fusion," in *Proc. IEEE Int. Conf. Robot. Autom.*, Nice, France, May 12–14, 1992, pp. 1720–1726.
- [44] L.-S. Wang, Y.-T. Chiang, and F.-R. Chang, "Filtering method for nonlinear systems with constraints," *IEEE Proc.-Control Theory Appl.*, vol. 149, no. 6, pp. 525–531, Nov. 2002.
- [45] S. Ko and R. R. Bitmead, "State estimation for linear systems with state equality constraints," *Automatica*, vol. 43, no. 8, pp. 1363–1368, 2007.
- [46] M. Tahk and J. L. Speyer, "Target tracking problems subject to kinematic constraints," *IEEE Trans. Autom. Control*, vol. 35, no. 3, pp. 324–326, Mar. 1990.
- [47] C. Yang and E. Blasch, "Kalman filtering with nonlinear state constraints," *IEEE Trans. Aerosp. Electron. Syst.*, vol. 45, no. 1, pp. 70–84, Jan. 2009.
- [48] J. De Geeter, H. Van Brussel, J. De Schutter, and M. Décrétion, "A smoothly constrained Kalman filter," *IEEE Trans. Pattern Anal. Mach. Intell.*, vol. 19, no. 10, pp. 1171–1177, Oct. 1997.
- [49] H. Michalska and D. Q. Mayne, "Moving horizon observers and observer-based control," *IEEE Trans. Autom. Control*, vol. 40, no. 6, pp. 995–1006, Jun. 1995.
- [50] B. O. S. Teixeira *et al.*, "Unscented filtering for interval-constrained nonlinear systems," in *Proc. IEEE Conf. Decis. Control*, Cancun, Mexico, Dec. 9–11, 2008, pp. 5116–5121.
- [51] D. Crisan and A. Doucet, "A survey of convergence results on particle filtering methods for practitioners," *IEEE Trans. Signal Process.*, vol. 50, no. 3, pp. 736–746, Mar. 2002.
- [52] S. Boyd and L. Vandenberghe, *Convex Optimization*. Cambridge, U.K.: Cambridge Univ. Press, 2004.
- [53] S. P. Drake, "Converting GPS coordinates $[\phi, \lambda, h]$ to navigation coordinates (ENU), Electr. Surveillance Res. Lab., Edinburgh, South Australia, Australia, Tech. Rep. DSTO-TN-0432, Apr. 2002.
- [54] H. Zhao and H. Chen, "Estimation of vehicle yaw rate and side slip angle using moving horizon strategy," in *Proc. 6th World Congr. Intell. Control Autom.*, Dalian, China, Jun. 21–23, 2006, vol. 1, pp. 1828–1832.
- [55] CarSim Educational Software. Mechanical Simulation Corporation, Ann Arbor, MI, USA, Jan. 2000.
- [56] M. Saha, B. Goswami, and R. Ghosh, "Two novel costs for determining the tuning parameters of the Kalman filter," 2011. arXiv:1110.3895.
- [57] M. Ananthasayanam, "Kalman filter design by tuning its statistics or gains?" in *Proc. Int. Conf. Data Assimilation*, Mumbai, India, Jul. 13–15, 2011.
- [58] D. Simon, *Optimal State Estimation: Kalman, H_∞ , and Nonlinear Approaches*. New York, NY, USA: Wiley, 2006.
- [59] Y. L. Murphey, R. Milton, and L. Kiliaris, "Driver's style classification using jerk analysis," in *Proc. IEEE Workshop Comput. Intell. Veh. Veh. Syst.*, 2009, pp. 23–28.
- [60] T. Flash and N. Hogan, "The coordination of arm movements: an experimentally confirmed mathematical model," *J. Neurosci.*, vol. 5, no. 7, pp. 1688–1703, 1985.
- [61] S. Mallat and W. L. Hwang, "Singularity detection and processing with wavelets," *IEEE Trans. Inf. Theory*, vol. 38, no. 2, pp. 617–643, Mar. 1992.
- [62] H. Damveld and R. Happee, "Identifying driver behaviour in steering: Effects of preview distance," in *Proc. Measuring Behav.*, Utrecht, The Netherlands, Aug. 28–31, 2012, pp. 44–46.
- [63] Y. Hassan and T. Sayed, "Effect of driver and road characteristics on required preview sight distance," *Can. J. Civil Eng.*, vol. 29, no. 2, pp. 276–288, 2002.
- [64] A. Grossmann, R. Kronland-Martinet, and J. Morlet, "Reading and understanding continuous wavelet transforms," in *Wavelets*. Berlin, Germany: Springer, pp. 2–20, 1989.
- [65] B. Jawerth and W. Sweldens, "An overview of wavelet based multiresolution analyses," *SIAM Rev.*, vol. 36, no. 3, pp. 377–412, 1994.
- [66] C. Torrence and G. P. Compo, "A practical guide to wavelet analysis," *Bull. Amer. Meteorol. Soc.*, vol. 79, no. 1, pp. 61–78, 1998.
- [67] Y.-U. Zhou and J.-Q. Cheng, "Wavelet transformation and its applications," *Acta Phys. Sin.*, vol. 37, pp. 24–32, 2008.



Changxi You received the B.S. and M.S. degrees from the Department of Automotive Engineering, Tsinghua University of China, Beijing, China, and the M.S. degree from the Department of Automotive Engineering, RWTH-Aachen University, Aachen, Germany. He is currently working toward the Ph.D. degree at the School of Aerospace Engineering, Georgia Institute of Technology, Atlanta, GA, USA.

His current research interests include system identification, aggressive driving maneuver, and control of (semi)autonomous vehicle.



Jianbo Lu received his B.S. degree in mechanical engineering from the Central South University, Changsha, China, and the M.S. degree in mechanical engineering from Arizona State University, and his Ph.D. degree in aeronautics and astronautics from Purdue University. He is currently a Technical Expert in advanced vehicle controls at Ford Motor Company, Dearborn, MI, USA. He holds more than 100 U.S. patents and numerous pending patent applications, and has published more than 70 journal and conference articles. His research interests include automotive controls and sensing, adaptive vehicle systems, driver assistance systems, smart mobility, and semiautonomous and autonomous systems.

Dr. Lu received the Henry Ford Technology Reward twice.



Panagiotis Tsiotras (SM'02) received the Eng.Dipl. degree in mechanical engineering from the National Technical University of Athens, Athens, Greece, the M.S. degrees in aerospace engineering from Virginia Tech, Blacksburg, VA, USA, and in mathematics from Purdue University, Lafayette, IN, USA, and the Ph.D. degree in aeronautics and astronautics from Purdue University.

He is currently the Dean's Professor in the School of Aerospace Engineering, and the Associate Director of the Institute for Robotics and Intelligent Machines at the Georgia Institute of Technology, Atlanta, GA, USA. His research interests are in optimal control, nonlinear control, and vehicle autonomy.

Dr. Tsiotras has been in the Editorial Boards of the IEEE TRANSACTIONS ON AUTOMATIC CONTROL (2009–2011), the IEEE CONTROL SYSTEMS MAGAZINE (2003–2009), and the *AIAA Journal of Guidance, Control, and Dynamics* (1999–2007). He received the NSF CAREER Award. He is a Fellow of the AIAA.